



THE UNIVERSITY *of* EDINBURGH

Edinburgh Research Explorer

In Vivo Modeling of Patient Genetic Heterogeneity Identifies New Ways to Target Cholangiocarcinoma

Citation for published version:

Younger, NT, Wilson, ML, Martinez Lyons, A, Jarman, EJ, Meynert, AM, Grimes, GR, Gournopoulos, K, Waddell, SH, Tennant, PA, Wilson, DH, Guest, RV, Wigmore, SJ, Acosta, JC, Kendall, TJ, Taylor, MS, Sproul, D, Mill, P & Boulter, L 2022, 'In Vivo Modeling of Patient Genetic Heterogeneity Identifies New Ways to Target Cholangiocarcinoma', *Cancer Research*, vol. 82, no. 8, pp. 1548-1559.
<https://doi.org/10.1158/0008-5472.CAN-21-2556>

Digital Object Identifier (DOI):

[10.1158/0008-5472.CAN-21-2556](https://doi.org/10.1158/0008-5472.CAN-21-2556)

Link:

[Link to publication record in Edinburgh Research Explorer](#)

Document Version:

Peer reviewed version

Published In:

Cancer Research

General rights

Copyright for the publications made accessible via the Edinburgh Research Explorer is retained by the author(s) and / or other copyright owners and it is a condition of accessing these publications that users recognise and abide by the legal requirements associated with these rights.

Take down policy

The University of Edinburgh has made every reasonable effort to ensure that Edinburgh Research Explorer content complies with UK legislation. If you believe that the public display of this file breaches copyright please contact openaccess@ed.ac.uk providing details, and we will remove access to the work immediately and investigate your claim.



Title: *In vivo* modeling of patient genetic heterogeneity identifies new ways to target cholangiocarcinoma.

Authors:

Nicholas T. Younger^{1, †, #}

Mollie L. Wilson^{1, #}

Anabel Martinez Lyons¹

Edward J. Jarman¹

Alison M. Meynert¹

Graeme R Grimes¹

Konstantinos Gournopoulos¹

Scott H. Waddell¹

Peter A. Tennant¹

David H. Wilson^{1, †}

Rachel V. Guest²

Stephen J. Wigmore²

Juan Carlos Acosta³

Timothy J. Kendall⁴

Martin S. Taylor¹

Duncan Sproul¹

Pleasantine Mill¹

Luke Boulter^{1, *}

*Corresponding Author: Dr Luke Boulter, MRC Human Genetics Unit, Institute of Genetics and Cancer, University of Edinburgh, EH4 2XU, UK. Email: luke.boulter@ed.ac.uk. Phone: +44 131 651 8636.

#both authors contributed equally to this manuscript

¹ MRC Human Genetics Unit, Institute of Genetics and Cancer, University of Edinburgh, EH4 2XU.

² Clinical Surgery, University of Edinburgh, Royal Infirmary of Edinburgh, Edinburgh, EH16 4SA.

³ Cancer Research UK Edinburgh Centre, Institute of Genetics and Cancer, Crewe Road South, Edinburgh, EH4 2XU.

⁴ Centre for Inflammation Research, University of Edinburgh, Edinburgh, EH16 4TJ.

† Current address: Centre for Inflammation Research, University of Edinburgh, Edinburgh, EH16 4TJ

Conflicts of interest: The authors do not have any conflicts of interest to declare.

Abstract:

Intrahepatic cholangiocarcinoma (ICC) is an aggressive malignancy of the bile ducts within the liver characterized by high levels of genetic heterogeneity. In the context of such genetic variability, determining which oncogenic mutations drive ICC growth has been difficult, and developing modes of patient stratification and targeted therapies remains challenging. Here we model the interactions between rare mutations with more common driver genes and combine in silico analysis of patient data with highly multiplexed in vivo CRISPR-spCas9 screens to perform a functional in vivo study into the role genetic heterogeneity plays in driving ICC. Novel tumor suppressors were uncovered which, when lost, cooperate with the RAS oncoprotein to drive ICC growth. Focusing on a set of driver mutations that interact with KRAS to initiate aggressive, sarcomatoid-type ICC revealed that tumor growth relies on Wnt and PI3K signaling. Pharmacological co-inhibition of Wnt and PI3K in vivo impeded ICC growth regardless of mutational profile. Therefore, Wnt and PI3K activity should be considered as a signature by which patients can be stratified for treatment independent of tumor genotype, and inhibitors of these pathways should be levied to treat ICC.

Significance: This work shows that, despite significant genetic heterogeneity, intrahepatic cholangiocarcinoma relies on a limited number of signaling pathways to grow, suggesting common therapeutic vulnerabilities across patients.

Introduction: Intrahepatic cholangiocarcinomas (ICC) are epithelial tumours of the bile duct comprised of malignant ducts surrounded by an extensive stroma(1). ICC driven by infection with the liver fluke, *Opisthorchis viverrini* is endemic in South East Asia and whilst historically seen as a rare malignancy in the West, sporadic, non-fluke associated disease has increased in incidence in the UK, Europe, and the USA over the last four decades. Currently, surgical resection is the only curative option for patients diagnosed with this cancer; however, of the ~30% of patients who have disease that is amenable to surgery, 70% of those patients relapse following resection(2). In patients where surgery is not an option, the standard of care is palliative chemotherapy, which extends life by ~3-6 months(3). Early studies using either patient ICC samples(4) or mouse models(5) demonstrated that oncogenic mutations in *Kras* (typically *Kras*^{G12D}) and loss of function mutations in *Trp53* cooperate to initiate tumour formation. Recent genomic data, however, has challenged whether mutations in this oncogene and tumour suppressor pair often co-occur in human ICC(6,7). Instead, these sequencing data suggest that alternate or less-frequent mutations cooperate with more dominant oncogenes (such as mutant *Kras*) to promote tumorigenesis. Deep sequencing of ICC has uncovered that a high level of genetic heterogeneity exists within patient ICC samples(8,9). Whilst a recurring set of mutations in canonical genes has been identified(1), many infrequent mutations have also been detected. The functional contribution of these infrequent *de novo* changes to affect disease progression and modulate therapeutic resistance or susceptibility remains unclear.

In order to identify and prioritise gain of function or loss of function mutations in a patient dataset of ICC, we use a computational pipeline, IntOGen(10), to generate a high-confidence list of candidate driver genes, of which 64 have not previously been assigned as being cancer drivers. To recapitulate the clonal competition observed in human tumorigenesis, we developed an *in vivo* CRISPR-SpCas9 system which simultaneously screens the candidate gene set against either *KRAS*^{G12D} or *NRAS*^{G12V} oncogenes. This identified a subset of genes in which human ICC-derived mutations genetically interact with RAS to initiate and accelerate ICC formation. Amongst these, we found that loss-of-function of Neurofibromin 2 (*Nf2*) interacts with mutant RAS to initiate tumour formation

independent of *Trp53* status, highlighting again that as seen in patient data, RAS mutant cells do not strictly rely on *Trp53*-loss to initiate ICC. Loss of *Nf2* results in the formation of aggressive and poorly differentiated sarcomatoid-type ICC. These tumors are driven by dysregulation of Wnt-PI3K signalling, highlighting a novel therapeutic avenue which could be used to target ICC growth.

Materials and Methods:

Identification and processing of genomic data from patient datasets:

Alignment and pre-processing of publicly available data: Exome-seq FASTQ files from Chan-on et al. (8) were downloaded from the European Nucleotide Archive with accession PRJEB4445. Exome-seq FASTQ files from Sia et al. (11) were downloaded from the Gene Expression Omnibus Database with accession GSE63420. TCGA BAM files were downloaded from the Genomic Data Commons after receiving access to individual patient BAM files. Input FASTQ files were aligned to the Hg19 reference genome. Duplicates were marked and base quality score recalibration was carried out and local indel realignment was performed. Ensemble variant calling was performed. TCGA data were input as reads which were aligned to the Hg38 reference so were re-mapped using the Hg38toHg19. IntOgen was run on each cohort individually, and then all combined. IntOgen outputs were used to build a network of known and inferred functional interactions and was clustered into modules by connection density and each module was annotated with pathway enrichments.

Evolutionary dependency (co-occurrence and mutual exclusivity) was scored using SELECT (version 1.6) with default parameters. The weighted mutual information (wMI) p-value was used for colour coding significance and false discovery rate (FDR) <0.1 used as multi-testing corrected threshold of significance. For the aggregate analysis of genes (“cosmic” and “other” groups), individual tumours were binary encoded as 1 if they contained a putative driver mutation in any gene of the corresponding gene list, and 0 otherwise.

Further experimental details about our computational approach can be found in supplementary materials.

Design and preparation of sgRNA plasmids for in vivo editing:

Generation of pooled sgRNA screening library: Oligonucleotides encoding sgRNAs targeting the set of predicted drivers were designed using spacer sequences from the mouse GeCKo V2 library

(**Supplementary Materials Table 1**)(12). Library-specific PCR retrieval arms (13) and our schematic for library preparation is described in **Supplementary Materials Table 1**. Complete sgRNA oligos for all target genes and control sequences were custom synthesised by Twist Biosciences. Purified amplicons were then digested with Esp3I, phosphorylated and ligated into the SB-CRISPR plasmid backbone.

Generation of single gRNAs: Single gRNAs (**Supplementary Materials Table 2 and Supplementary Figure 3A**) were cloned into SB-CRISPR plasmids kindly provided by Professor Dr Roland Rad (LMU Munich). SB-CRISPR was digested with Esp3I or BbsI.

Animal work: All animal work was performed under the UK Home Office project license held by Dr Luke Boulter (PFD31D3D4). Animals were maintained in colonies in 12h light-dark cycles and were allowed access to food and water *ad libitum*.

Hydrodynamic tail vein injection: Female, FVB/N mice from Charles River, UK and were used at 4-6 weeks of age. For the hydrodynamic tail vein injection, animals were injected with a physiological saline solution (10% w/v) containing plasmids into the lateral tail vein. The typical injection contained 6µg of PGK-SB13, 20ug of CAG-Kras^{G12D} or CAG-Nras^{G12V} and 20µg of SB-CRISPR gRNA plasmid. In models that relied on a combination of gRNA plasmids, plasmids were dissolved to a maximum concentration of 20µg and were mixed such that they were balanced pools of each gRNA. For screening studies, the gRNA library was injected at 20ug and we determined gRNA representation by Sanger sequencing prior to injection and plotted the GINI index for each library (**Supplementary Figure 3B**).

Keratin-19-CreER^T;Pten^{flox/flox};Trp53^{flox/flox};R26R^{LSLtdTomato} mice (KPPTom): Keratin-19-CreER^T mice (Jax: 026925) were crossed with animals containing floxed alleles of *Pten* (Jax: 006440) or *Trp53* (Jax: 008462) and a silenced tdTomato reporter targeted to the Rosa26 locus (Jax: 007908) . All animals in this study are heterozygous for Keratin-19CreER^T, homozygous for *Trp53*^{flox} and *Pten*^{flox} alleles and

homozygous for $R26R^{LSLdTomato}$. Mice received three doses of 4mg of tamoxifen by oral gavage and followed by 400mg Thioacetamide in their drinking water. All mice were male.

Therapeutic dosing of animal models: Animals bearing $KRAS^{G12D};gRNA^{Nf2};gRNA^{Trp53}$ tumours were randomised using graphpad online randomisation tool and dosed with either vehicle alone (10% DMSO, 40% PEG300, 5% Tween-80 and 45% saline), 5mg/Kg LGK974, 50mg/Kg Pictilisib or a combination of the two daily starting 7d following hydrodynamic injection. KPPTom animals were given tamoxifen and Thioacetamide (as detailed above) and at four weeks were given either vehicle alone (10% DMSO, 40% PEG300, 5% Tween-80 and 45% saline) or a combination of 5mg/Kg LGK974 and 50mg/Kg Pictilisib for 4 weeks. All animals were housed in colonies of five animals.

Isolation of RNA and DNA: Both DNA and RNA extraction used 50-100mg of snap frozen tissue. DNA was extracted from tissue using the DNeasy Blood and Tissue Kit (QIAGEN) as per the manufacturer's instructions. RNA was extracted using TRIzol RNA Isolation Reagent (Invitrogen), precipitated with chloroform and cleaned up using the RNeasy Mini Kit (QIAGEN). For sequencing applications DNA and RNA quality (RIN score) was quantified using the Agilent 2100 Bioanalyzer. A minimum RIN threshold of 8 was used for RNA-seq.

RNA Sequencing: Libraries were prepared from total-RNA following rRNA depletion. rRNA-depleted RNA was then DNase treated and purified prior to fragmentation Libraries were quantified by fluorometry and assessed for quality and fragment size using the Agilent Bioanalyser Sequencing was performed using the NextSeq 500/550 High-Output v2.5 (150 cycle) Kit on the NextSeq 550 platform (Illumina Inc). Libraries were combined in an equimolar pool based on Qubit and Bioanalyser assay results and run across a single High Output v2.5 Flow Cell.

RNA sequencing data processing and analysis: The primary RNA-Seq processing, quality control to transcript-level quantitation, was carried out using `nf-core/rnaseq v1.4.3dev` (<https://github.com/ameynert/rnaseq>)(14).

DNA exome sequencing: Libraries were prepared from genomic DNA (gDNA) and was sheared to achieve target DNA fragment sizes of between 150 and 200bp. DNA fragments were processed as adapter-ligated libraries and were purified. 750ng of each prepared gDNA library was hybridised to probes covering the mouse exome and hybridised DNA-probes were amplified to apply unique indexing primers. **Library QC:** Libraries were quantified by Qubit and sequencing was performed using the NextSeq 500/550 High-Output v2.5 (150 cycle) Kit on the NextSeq 550 platform (Illumina Inc). Libraries were combined in a single equimolar pool and run on a High-Output v2.5 Flow Cell.

CRISPR/Cas9-editing validation and Structural Variant calling: DNA sequences from exome-sequencing of tumours arising from the RAS^{G12}-library screens and were aligned to the FVB mouse reference genome; subsequently, indels within 50bp upstream or downstream of sgRNA target sites were called. To determine if indels were likely due to SpCas9 activity, the interval of each indel was observed using Integrative Genomics Viewer(15), and overlain with sgRNA library binding sites. Further information on identifying the outcome of CRISPR editing is detailed in the supplementary material.

Data curation and deposition: All RNA and Exome sequencing data pertaining to this manuscript is deposited on the NCBI Gene Expression Omnibus (GEO) as accession number GSE190770.

Histology and Immunohistochemistry: Livers were perfused with phosphate buffered saline and dissected into 10% neutral buffered formalin. Fixed tissue was processed in wax blocks and sectioned 4 µm thick. Sections for immunostaining were dewaxed in xylene and rehydrated. Following antigen retrieval and sections were incubated with primary and secondary antibodies as detailed in **Supplementary Materials Table 3**. Histological assessment was undertaken by a consultant liver histopathologist working at the national liver transplant centre (TJK) with experience in the comparative pathology of animal models of primary liver cancer.

FUnGI immunostaining and clearing: We adapted a previously published protocol for FUnGI staining and imaging(16). 8mm cores were are taken from liver and cancer tissue and sectioned at 200µm intervals using a Krumdeick Tissue Slicer and fixed in formalin. Tissues were blocked and incubated

over night with primary and secondary antibodies in a series of permabilising washes before being cleared in FUnGI solution which contains high levels of fructose. Clarified tissues are incubated with DAPI and mounted in FUNGI for confocal analysis.

Quantification of tumour burden: Histological sections containing tumours were scanned using a Nanozoomer slide scanner with a 40X objective lens. Files were then imported into QuPath (<https://qupath.github.io>) and tumour tissue was manually annotated. Tumour Burden represents the area of tissue occupied by tumour and number is the number of discrete tumours in the tissue. All tumour analysis was blinded.

Reverse phase protein arrays: Snap frozen, dissected tumour tissue was provided to the Human Tumour Profiling Unit (HTPU) at the Cancer Research UK Edinburgh Centre. The target proteins analysed by RPPA are listed in **Supplementary Materials Table 4**. Reverse Phase Protein Array (RPPA) analysis was carried out using established protocols for nitrocellulose-based arrays(17). Slide images were acquired using an InnoScan 710-IR scanner (Innopsys) with laser power and gain settings optimised for highest readout without saturation of the fluorescence signal. The relative fluorescence intensity of each array feature was quantified using Mapix software (Innopsys).

Statistical Analysis: All experimental groups were analysed for normality using a D'Agostino–Pearson Omnibus test. Groups that were normally distributed were compared with either a two-tailed Student's t test (for analysis of two groups) or using one-way ANOVA to compare multiple groups, with a post hoc correction for multiple testing. Non-parametric data were analysed using a Wilcoxon–Mann–Whitney U test when comparing two groups or a Kruskal–Wallis test when comparing multiple non-parametric data. Throughout, $P < 0.05$ was considered significant. Data are represented as mean with S.E.M. for parametric data or median with S.D. for non-parametric data.

All figures were laid out with Adobe Illustrator and graphics were created with BioRender.com.

Results:

Identifying candidate causative mutations that drive ICC growth: Intrahepatic cholangiocarcinoma contains a range of infrequently mutated genes without known function. Identifying a consensus group of driver mutations in ICC using exome and genome sequencing has been challenging, due in a large part to tissue availability. Nonetheless, a number of studies have demonstrated recurrent ICC mutations including neomorphic alterations in *IDH1* and *IDH2*, loss-of-function mutations in *PBRM1*, *BAP1*, *TP53*, *ARID1A* and gain-of-function mutations in *KRAS*. Despite their identification, the presence of these mutations in a tumour is not a strong predictor of therapeutic outcome(18,19) and for approximately 30% of ICC patients a driver mutation cannot be identified(20).

To determine whether all patient tumours contain potential driver mutations, we used a computational pipeline based around the driver prediction tool IntOGen(10). This method utilises a combination of functional impact bias (OncodriveFM), spatial clustering (OncodriveCLUST) and corrected frequency (MutSigCV) to define whether particular genomic regions have a mutational rate beyond that which is expected, have a bias towards clustered mutations or those which are likely to impact functional domains, such as those that are regulatory or catalytic (summarised in **Supplementary Figure 1**). Having filtered out hypermutated samples (**Supplementary Table 1**), we used this pipeline to analyse the variants identified in the genomes of 277 sporadic and fluke-associated ICCs from four distinct studies(7,11,21,22), summary information on the aggregated cohort can be found in **Supplementary Figure 2A-H** and **Supplementary Table 2**). Following processing, 55% of samples (N=152) carried ≥ 2 predicted drivers whilst 18% (N=50) carried none (**Figure 1A**, and **Supplementary Table 3**). Of these predicted driver mutations, approximately one third of mutations were already known to occur in ICC or were present in genes in the COSMIC database (**Figure 1B**). The remaining two thirds of mutations were novel and occurred in fewer than 8% of ICC cases. Indeed, the majority of novel mutations were only found in 3-4 patients, corresponding to $\sim 1.5\%$ of the patient cohort (**Figure 1C**, **Supplementary Table 4** and

Supplementary Table 5). To explore whether these low-frequency predicted drivers are involved in common pathways or processes, networks were constructed based on known and predicted physical interactions⁽²³⁾ and clustered into modules based on connection density⁽²⁴⁾ (**Figure 1D**). This produced a network with 6 modules containing a mix of known in ICC, COSMIC, and novel genes. Gene ontology analysis was performed on the modules to ascertain the biological processes in which each module may participate (**Supplemental Table 6**). Finally, we sought to determine whether, based on our mutations as defined through IntOgen, we could define the genetic interactions between mutations in this patient dataset. Within our group of canonical driver mutations, we found that (with the exception of *KRAS* and *TP53*) there is a consistent and high level of mutual exclusivity between canonical driver genes, suggesting that the recurrent mutations found across studies are not interdependent for ICC initiation and growth (**Figure 1E**). Interestingly, when we expanded this analysis to include COSMIC mutations and novel mutations (those that recur ≥ 15 times within our dataset *BRAF*, *PIK3CA*, *EPHA2* and *SMAD4* are individually identified and those with ≤ 15 occurrences within this set are grouped as “cosmic” and novel are defined as “other”) we find distinct patterns of co-occurrence and mutual exclusivity which support the idea that there are *bona fide* genetic interactions between canonical driver genes (e.g. *KRAS*) and the large group of novel, infrequently mutated genes identified by IntOgen (**Figure 1F**).

***In vivo* CRISPR-SpCas9 screening identifies novel tumour suppressors in RAS driven ICC.** Clonal analysis of patient ICC has failed to identify a consensus mutational route through which tumours progress(25) or epistatic mutations that functionally interact to drive tumour initiation and growth. Relatively low sample number and high genetic heterogeneity in ICC exacerbate the difficulties with this type of associative analysis.

To overcome these limitations and define which candidate drivers are functionally capable of initiating ICC, we developed an *in vivo* screening approach that allowed us to functionally prioritise ICC driver mutations (**Figure 2A**). Previous work using multiplex-mutagenesis in the liver has demonstrated that editing specific genomic loci in hepatocytes can give rise to ICC, albeit using a relatively limited pool of gRNAs, targeting 10 genes(26). In this system, naked DNA is delivered to the liver using a high pressure, hydrodynamic injection into the lateral tail-vein of mice, an approach that has been used in the past to deliver cDNAs coding oncogenes(27,28). When paired with CRISPR-SB plasmids containing sgRNAs and SpCas9 flanked between two Sleeping Beauty (SB) inverted terminal repeats, and a plasmid expressing Sleeping Beauty (SB) transposase, it is possible to edit *in vivo* endogenous genes in hepatocytes in a mosaic manner(29). Using the CRISPR-SB system as a starting point, we generated a large-scale multiplexed CRISPR-SpCas9 plasmid library (known hereafter as ICC^{lib}) containing triplicate gRNAs targeting 91 mouse homologues of our putative, patient-derived ICC driver genes identified through our *in silico* approach. Five genes (*KRTAP12-1*, *RBML1*, *RBML*, *SPANXD* and *ZNF181*) from our human dataset had no identifiable murine orthologue, and so were excluded from further analysis (**Supplementary Figure 3A and 3B**).

Using this CRISPR-SpCas9 system we randomly introduced CRISPR-SpCas9 targeted mutations into these candidate “patient-led” ICC genes in otherwise wild-type mice to determine which loss of function mutations are necessary for tumour initiation and determine whether any loss of function mutations interact to drive ICC formation. The ICC^{lib} alone failed to induce any tumours in mice after 10 weeks suggesting that within this timeframe these loss-of-function mutations alone are

insufficient to initiate cancer. Gain-of-function mutations in *KRAS* and *NRAS* have been previously described in ICC(8) and through our IntOGen analysis, we similarly identified recurrent mutations in both of these genes (*KRAS* 18.05% and *NRAS* 2.88%, **Supplementary Table 4**). In experimental models, expression of mutant RAS in the adult liver is weakly oncogenic and normally insufficient to initiate ICC formation; rather, mutant cells undergo oncogene-induced senescence and are removed from the liver by immune clearance(30). Therefore, we co-expressed cDNAs of GFP tagged $KRAS^{G12D}$ or $NRAS^{G12V}$ with our ICC^{Lib} to determine whether any of the loss-of-function mutations introduced via the ICC^{Lib} synergise with mutant RAS proteins to promote ICC initiation. Within 10 weeks, mice that received either $KRAS^{G12D}$ or $NRAS^{G12V}$ and loss-of-function mutations induced by the CRISPR-SpCas9 containing ICC^{Lib} developed macroscopic and multifocal cancer; this was accelerated in $KRAS^{G12D}$ mice, which developed symptomatic liver cancer in 8 weeks (**Figure 2B**). In those mice that developed cancer, multiple tumours formed per mouse (**Figure 2C**) which were histologically aggressive adenocarcinoma with a poorly differentiated cholangiocellular morphology. Importantly, these tumours express GFP (**Supplementary Figure 4A**), denoting that they continue to express the $KRAS^{G12D}$ or $NRAS^{G12V}$ constructs, and the cholangiocyte marker Keratin-19, which is constrained to the biliary epithelium in normal livers (**Supplementary Figure 4B**). Together, these data demonstrate that mutant Ras ($NRAS^{G12V}$ or $KRAS^{G12D}$) can interact with at least one loss-of-function mutation generated by the gRNAs contain in the ICC^{Lib} to initiate ICC *in vivo*.

To determine which CRISPR-SpCas9 mutational events cooperated with $KRAS^{G12D}$ or $NRAS^{G12V}$ and lead to the emergence of liver cancer, whole exomes were sequenced from 14 $KRAS^{G12D}$ and 10 $NRAS^{G12V}$ driven tumours. All indels within 50bp of a sgRNA target site were manually inspected to determine whether they were Cas9-induced or of spontaneous origin. Almost all indels had start or end positions approximately 3bp upstream of the SpCas9 protospacer adjacent motif (PAM) sequence strongly indicating that they are a consequence of CRISPR-SpCas9 editing (**Supplementary Figure 5A**). Our data shows that tumours acquired multiple CRISPR-SpCas9-induced lesions; $KRAS^{G12D}$ tumours contained an average of 7.5 ± 1.19 mutations and in $NRAS^{G12V}$ tumours there were on

average 7.7 ± 2.59 CRISPR-SpCas9 induced mutations (**Supplementary Figure 5B**). Across both $Kras^{G12D}$ and $Nras^{G12V}$ screens, 66 of the 91 predicted drivers targeted with the ICC^{Lib} were mutated and 27 of these were shared between $NRAS^{G12V}$ and $KRAS^{G12D}$ tumours (**Figure 2D** and **Supplementary Figure 6**). The most common CRISPR-SpCas9 mutation we identified was unsurprisingly in *Trp53*, reiterating the ability of cells with *Trp53*-loss-of-function mutations to overcome RAS-induced senescence(31). We also found recurrent CRISPR-induced indels from both $NRAS^{G12V}$ and $KRAS^{G12D}$ screens in genes whose loss has been linked to ICC, but which have not previously been shown to genetically interact with mutant RAS in this cancer including *Brca2*, *Nf2* and *Plk2* (**Figure 2D**).

***Nf2*-loss interacts with KRAS^{G12D} and *Trp53*-loss to promote sarcomatoid phenotypes in ICC.** Our data demonstrate that loss of numerous genes mutated at low frequency in human ICC potentially interact with activating NRAS^{G12V} and KRAS^{G12D} mutations to promote ICC initiation *in vivo*. These data and those of others has demonstrated that *KRAS* mutations occur more frequently in ICC than those in *NRAS*(9), therefore we prioritized validating loss-of-function mutations that genetically interact with KRAS^{G12D}. From our screen, we identified which mutations in patients have the potential to initiate the formation of Ras-induced ICC, therefore we set about to define whether any particular mutation (or set of mutations) alters the phenotype of these cancers. RNA sequencing analysis of our ICC^{lib} screen tumours showed that, on the whole, tumours transcriptionally clustered closely to each other by Principal Component Analysis (PCA) and were transcriptionally similar to tumours generated by expressing both KRAS^{G12D} and deleting *Trp53* (**Figure 2E**). Furthermore, our screen tumours were transcriptionally distinct from normal bile ducts. However four tumours in our screen transcriptionally segregated from all other tumours; all contained SpCas9/CRISPR-induced mutations in both *Trp53* and *Nf2*. In fact, of the 14 cancers from our screen that we exome sequenced, four of the five containing *Nf2*-mutations segregated away from the main cluster (**Figure 2E**), suggesting that the addition of a mutation in *Nf2* can functionally cooperate with *Kras*^{G12D} and *Trp53* mutations and affects the phenotype of ICC. NF2 is also known as Merlin and has a well-defined role in the Hippo/LATS signalling pathway, where it negatively regulates pathway activation through the phosphorylation of *Mst1/2*; however, NF2/Merlin is also known to interact with a number of other signalling pathways including PI3K and Wnt signalling(32). We elected to investigate the genetic interaction of *Nf2*, *Trp53* and *Kras*^{G12D} further, by generating gRNAs to specifically target and disrupt the *Nf2* and *Trp53* loci (or a non-targeting control, gRNA^{scrm}) which were then co-injected hydrodynamically with our KRAS^{G12D} expressing construct in order to define whether loss of these tumour suppressors can specifically cooperate with KRAS^{G12D} to promote tumour initiation. *Trp53*-loss and *Nf2*-loss were both capable of overcoming the senescence inducing effects of *Kras*^{G12D} expression in the liver and mice developed lethal tumours within 8 weeks following injection (**Figure**

3A). In the presence of KRAS^{G12D}, the singular deletion of either *Trp53* or *Nf2* resulted in large discrete tumours. However, dual loss of *Trp53* and *Nf2* resulted in cancers that were highly aggressive and invasive, which had a median survival of 14 days compared to 39 and 41 days in singular *Nf2*-deleted and *Trp53*-deleted tumours, respectively (**Figure 3A**). Tumours that lacked both *Trp53* and *Nf2* were highly diffuse and covered less liver area compared to both single gene deletions; however, the number of tumours that formed was significantly higher in *Trp53*;*Nf2* co-deleted tumours, suggesting that mutations in these two tumour suppressors may synergise in cancer and are not functionally redundant (**Figure 3B** and **3C**). Rather, the co-deletion of *Trp53* and *Nf2* enables the increased retention of mutant Kras^{G12D}-expressing cells within the liver. This retention leads to more cancers forming and that the accelerated mortality seen in animals bearing *Trp53*;*Nf2* co-deleted tumours is likely due to the number of tumours that are able to form, rather than due to their size. Histopathologically, the *Trp53*;*Nf2* co-deleted cancers are highly invasive with CK19 and GFP (KRas^{G12D}-expressing) immunopositive cells migrating throughout the liver (**Figure 3D**, **Supplementary Figure 7**) and represent a model to study the biology of invasive, sarcomatoid ICCs which migrate along the ducts and invade the liver(33). Rather than those ICCs which are mass forming (and which have been previously modelled in mice), sarcomatoid ICC whilst rare, has a very poor prognosis with a survival of weeks to months following diagnosis(34). In mouse, these *Trp53*;*Nf2* co-deleted sarcomatoid cancers grow rapidly, however we do not observe perineural or microvascular invasion, nor did we see enlarged lymph nodes in these mice suggesting the main cause of lethality is loss of functional liver capacity rather than the exit of cells from the tumour mass.

To determine the transcriptomic differences driving this aggressive phenotype in *Trp53*;*Nf2* co-deleted cancers when compared to individual *Trp53* or *Nf2* deleted tumours, we undertook bulk RNA sequencing of tumours with Kras^{G12D};*Trp53*^{KO}, Kras^{G12D};*Nf2*^{KO} or Kras^{G12D};*Trp53*^{KO};*Nf2*^{KO} genetic profiles. Sarcomatoid, *Trp53*;*Nf2* co-deleted tumours are transcriptionally distinct from cancers containing either *Trp53* or *Nf2* deletions alone based on PCA (**Supplementary Figure 8A** and

Supplementary Table 7). By comparing the up- and down-regulated genes in *Trp53* vs *Trp53;Nf2* co-deleted tumours against the changes found in *Nf2* vs *Trp53;Nf2* co-deleted tumours, we identified enrichment in signatures for Wnt signalling and Cadherin signalling using PANTHER (**Supplementary Figure 8B**) in our model of sarcomatoid ICC. However, we did not find a transcriptional signature for Hippo signalling (which we would anticipate based on NF2's canonical role in this pathway), nor could we identify YAP positive cells within the *Nf2*-deleted tumours, rather YAP-positive cells are only found adjacent to the tumour mass. Together, these data indicate that *Nf2*-loss in these tumours fails to activate Hippo signalling (**Figure 3E** and **Supplementary Figure 8B-C**). Previous work from our group has shown that Wnt signalling promotes ICC growth in the absence of classical Wnt pathway "activating mutations"(35). In *Trp53;Nf2* co-deleted cancers, we observe upregulation of *Wnt9b* and suppression of inhibitors of Wnt signalling *Nkd2* and *Sfrp2* suggesting that alterations in ligand levels and negative regulators of Wnt signalling are important mediators of ICC progression and that these cancers form independent of core Wnt-activating mutations in *Apc*, *Axin2* and *Ctnnb1*(36). Interestingly, sarcomatoid ICC in patients displays changes in cadherin expression, though it is not clear whether these changes are causative for the aggressive sarcomatoid phenotype(37). In our model, we found transcriptional suppression of a range of cadherins and proto-cadherins that have been also implicated in Wnt regulation(38).

As there are few targeted treatments for poorly differentiated ICC, we screened our models driven by KRAS^{G12D}-expression and either *Trp53*-loss, *Nf2*-loss or a combination of the two for activated and pharmacologically targetable signalling pathways using highly multiplexed Reverse Phase Protein Arrays (RPPAs). Deletion of *Nf2* (either alone, or in combination with *Trp53*) results in increased inhibitory phosphorylation of GSK3 β and activation of β -catenin signalling when compared to KRAS^{G12D} driven tumours lacking *Trp53* alone. These changes demonstrate that in *Nf2*-mutant cancers the canonical Wnt signalling pathway is highly activated and that the alterations in levels of Wnt ligands and inhibitors found at the transcriptional level translate into increased pathway activation (**Figure 3F**). Furthermore, when *Trp53* and *Nf2* are concurrently deleted, the proportion of

AKT that is phosphorylated at Serine-473 significantly increases (**Figure 3G**), indicating that within these $Kras^{G12D};Trp53^{KO};Nf2^{KO}$ cancers signalling via AKT is also elevated. Histologically, β -catenin is found within all KRAS-driven cancers (**Figure 3G**) but the dephosphorylated (active) form of the protein is increased in protein lysates from $Kras^{G12D};Trp53^{KO};Nf2^{KO}$ tumours (Figure 3H). These data suggest that concurrent pAKT and Wnt activity promote the development of sarcomatoid ICC and that this combination of mutations is also sufficient to suppress apoptosis in these cancer cells (**Supplementary Figure 9A and 9B**) thereby promoting the development of cancer in the liver which rapidly becomes lethal. To test whether the aggressiveness of $Trp53;Nf2$ mutated ICC is dependent on Wnt and AKT signalling directly, we treated mice bearing $KRAS^{G12D};Nf2;Trp53$ -KO tumours with an inhibitor of Porcupine (LGK974), which reduces Wnt ligand secretion by preventing palmitoylation of Wnt ligands and a PI3K inhibitor, Pictilisib, which prevents the conversion of PIP_2 into PIP_3 and thereby reduces AKT phosphorylation. Animals were given sarcomatoid ICC (by a hydrodynamic injection of $KRAS^{G12D};gRNA^{Nf2};gRNA^{Trp53}$) and at seven-days following tumour initiation were randomised to receive vehicle, LGK974, Pictilisib or a combination of the two compounds (combination treatment), summarised in **Figure 3I**. Both LGK974 and Pictilisib significantly improve survival of tumour bearing mice compared to animals treated with vehicle alone (median survival of 19 days in vehicle treated versus 21 days in LGK974-treated ($p=0.0015$) and 22.5 days in Pictilisib-treated animals ($p=0.0058$), respectively). Wnt inhibition and PI3K inhibition performed similarly, with no statistically significant difference in survival outcomes when used as single agents (**Figure 3J** and **Supplementary Figure 10A-C and Supplementary Table 8**). In combination, LGK974 and Pictilisib improve median survival from 19 days to 25.5 days (**Figure 3J**), significantly ($p<0.001$) reducing mortality compared to single treatments (**Supplementary Figure 10D-F**) and demonstrating that co-inhibition of Wnt and PI3K signalling is an effective treatment in sarcomatoid tumours that lack classical Wnt and PI3K activating mutations (i.e mutations in *APC*, *CTNNB1* and *PI3KCA*).

Wnt and PI3K/AKT represent a conserved mechanism by which distinct pathological subtypes of ICC grow. From previous transcriptomic studies of ICC, it is possible to identify a subgroup of patients with high Notch pathway activity and who would be sensitive to treatment with γ -secretase-inhibitors(39). We therefore sought to identify whether there is a group of ICC patients who could be sensitive to co-inhibition of Wnt and PI3K signalling. In 104 transcriptomes from ICC patients(21), there is a high level of correlation ($r=0.690$, $P<0.0001$) between those with a high expression of genes associated with Wnt signalling and high expression of genes associated with AKT signalling (**Figure 4A** and **Supplementary Table 9**). Therefore, we considered whether the activation of Wnt and PI3K signalling is a more universal process in ICC formation and sought to address whether these pathways are recurrently activated in ICC lacking *RAS* mutations, particularly given the majority of ICC patient cancers (79.07%) do not carry a mutation in either *Kras* or *Nras* (**Supplementary Table 4**).

To test this, we deleted *Trp53*, which is the most common mutation in our patient cohort, mutated in 19.13% of cases (**Figure 1C**) and *Pten* specifically in biliary epithelial cells using a *Keratin19-Cre^{ERT}* knock-in mouse line. While *Pten* mutations were not found in our computational analysis of ICC, loss of *Pten* recapitulates the effects of PI3KCA mutations(40) (which is mutated in 5.4% of patients in our cohort, **Figure 1C**) resulting in the accumulation of PIP₃ and AKT activation. Furthermore, previous studies have demonstrated that *Pten* loss potentiates ICC formation on the background of steatosis (fatty liver) and interacts with *Smad4*-loss to initiate liver cancer(41,42). Concurrently, with *Trp53* and *Pten* deletion, recombined cells were labelled with tdTomato (from here on in this line is known as the KPPTom line, **Figure 4B**). These animals are then challenged with chronic administration of Thioacetamide, a hepatotoxin that has been used to induce ICC in other models but is not itself mutagenic(43). Within four weeks of Thioacetamide treatment, mice develop moderate to well-differentiated cholangiocellular neoplasms around the portal tracts within the liver, which are lineage traced with tdTomato, confirming that they have arisen from the biliary epithelium (**Figure 4C**). Using FUnGI imaging(44), we found that small, tdTomato positive ICC

microfoci (~200µm across) can be identified forming from the ducts by 4 weeks and in normal 2D histology appear as small clusters of lineage traced ducts, with an atypical luminal structure. These cancerous microfoci grow progressively over 8 weeks and occupy approximately 22% of the liver (**Figure 4D**). In this model, the deletion of *Trp53* and *Pten* alone are insufficient to promote tumour initiation, instead the addition of a damaging agent (Thioacetamide) and the induction of ductular regeneration are essential for tumour initiation (**Figure 4D**). Tumours from KPPTom mice are positive for dephosphorylated (active) β -catenin, which localises to the cytoplasm and nucleus of cancer cells, as well as phosphorylated AKT^{Ser647} (**Figure 4E**). As KPPTom mice show both Wnt and PI3K/AKT activity, we treated them with LGK974 (to inhibit Wnt signalling) and Pictilisib (to inhibit Pi3K signalling) at four weeks following tumour induction (i.e. the start of Thioacetamide treatment), and a time point at which we know that there is ICC forming in the liver (**Figure 4F**), in order to determine whether a model of well-differentiated ICC is susceptible to co-inhibition of these pathways. Following treatment, the number of tdTomato-positive cancer cells was significantly reduced (by 68.3%) when compared to control vehicle treated animals (**Figure 4G** and **4H**). Indeed when treated with LGK974 and Pictilisib, only 33% of KPPTom mice developed ICC, whereas in the vehicle treated cohort, 80% of KPPTom mice contained cancerous lesions (**Figure 4I**).

Discussion:

Intrahepatic cholangiocarcinoma (ICC) is highly complex at the genetic(25) and cellular levels. While a number of candidate mutations have been identified that can be pharmacologically targeted(19), these have not led to a broadly applicable treatment. Moreover, the presence of these mutations does not necessarily predict therapeutic responsiveness in patients with ICC and only a subset of these patients respond to targeted therapy(20). Consequently, there is a clinical necessity to identify the mechanisms that ICC uses to grow and define whether these processes can be used in patient stratification and targeted treatment. In order to define a targeted therapeutic approach that can be used in treating a specific cohort of ICC patients, we need to understand whether the genetic complexity found in ICC ultimately translates to phenotypic diversity or whether ICC relies on a limited number of signalling cascades to grow in spite of this genetic complexity.

The identification of causative mutations in ICC is fraught with complications. Historically these studies relied heavily on identification of genes with recurrent consensus mutations in patients. This approach has been severely limited by the relatively small number of ICC samples available. Increasing sample size by pooling data from across published cohorts and combining this with a driver prediction pipeline that puts less weight on mutation recurrence within a population, but rather concentrates on the patterns and predicted effects of mutations(10) enabled us to identify an expanded set of candidate mutations in ICC that have the potential to act as oncogenes.

Whilst able to predict novel candidate oncogenic mutations, the approach described here is not able to infer which mutations act in epistasis to promote tumour formation. To overcome this limitation we developed an *in vivo*, highly multiplexed CRISPR-SpCas9 screening approach. Our strategy builds on previous work demonstrating that smaller gene-editing libraries can be used to define which tumour suppressors are important for ICC initiation and build on a substantial body of work identifying which oncogenes are essential for the formation of cancer cells in the liver(26), particularly KRas which has previously been used to define the responsiveness to MEK inhibition in ICC(45). Rather than using whole genome screening, we biased our libraries to ensure that they

targeted genes mutated in ICC patients. Using this strategy has enabled us to define a range of putative tumour suppressors that cooperate with gain-of-function *Ras*-mutations to overcome RAS-induced senescence and initiate tumour formation. We validated that one of these, Neurofibromin-2 (*Nf2*, or Merlin) can act as an important factor in the initiation of RAS-driven ICC and we show increased penetrance and aggression of RAS-driven ICC when *Nf2*-loss is combined with *Trp53*-loss. The phenotypes of these *Nf2*-mutant tumours are highly sarcomatoid, the cancer cells have a more spindle-like morphology and are dispersed throughout the liver. Perhaps this is unsurprising given the role of NF2 in maintaining contact inhibition and restricting cell migration in the presence of Ras mutations, as NF2 has been implicated in the fine tuning of Ras signalling in Schwann cells(46). However, loss of *Nf2* has not been shown to be sufficient to cooperate with Ras and drive tumour formation independent of other accessory mutations and while loss of *Nf2* has been previously shown to promote the formation of mixed HCC and ICC when it is deleted from the liver during development(47), it was unclear whether *de novo* somatic *Nf2* mutations interact with other ICC-relevant mutations *in vivo*. In addition to Hippo signalling, NF2 has also been implicated in the regulation of a number of other signalling pathways(48). We found that Wnt and PI3K signalling are recurrently de-regulated following *Nf2*-loss in our mouse model, leading us to identify co-inhibition of Wnt and PI3K as a potent therapeutic combination in reducing ICC growth. In cancer, Wnt signalling is classically activated by mutations in a core set of genes(49). In Hepatocellular Carcinoma (HCC) for example, the Wnt signalling pathway is activated via gain-of-function mutations in β -catenin and is known to directly promote tumour progression in mice(50). No such classical activating mutations have been found in ICC genome sequencing (with the exception of rare RNF43 mutations(8)) despite a number of descriptions of ICC being a Wnt-high tumour(35). Our data indicates that other mutations can similarly potentiate Wnt signalling likely by enabling cancer cells to enter a state that is permissive to ligand reception. Critically, we show that Wnt signalling is part of a signalling network that also involves the activation of AKT, which in ICC can be activated through a number of mechanisms and is known to affect the stability of β -catenin by inhibitory

phosphorylation of GSK3 β . Furthermore, Wnt (porcupine) inhibitors and PI3K inhibitors are currently in clinical trials for other solid malignancies and our data supports recent findings in pancreatic cancer(51), that treating patients with Wnt and PI3K inhibitors provides an attractive therapeutic route to reduce tumour burden.

Conclusions:

Our data demonstrates the importance of understanding the function of rare mutations in ICC and shows that these low-frequency mutations not only influence the outcome of more common driver mutations, but also can lead us to define applicable therapeutic strategies that can be used to develop personalised approaches which could be applied clinically to stratify patients and treat ICC of divergent genotypes based on the signalling pathways that are deregulated in these cancers.

Ethics approval and consent to participate: All human data included in this manuscript comes from previously published, consented studies. Animal work performed here is approved by the UK Home Office licence provided to LB. **Availability of supporting data:** All -omics data is deposited in publically accessible databases and all other datasets used and analysed during the current study are available within the manuscript and its additional files. **Funding:** LB is funded by The Wellcome Trust (207793/Z/17/Z), AMMF (2016/108, 2017/115) and Cancer Research UK (C52499/A27948). **Authors' contributions:** NTY, MLW designed and performed experiments, analysed data and prepared the manuscript. AMM analysed data. KG, AML, EJJ, SHW, PAT and DHW performed experiments and analysed data. RVG, SJW, JCA provided tissue and reagents. TJK provided pathological support, DS (who is supported by a Cancer Research UK Career Development fellow (reference C47648/A20837) and an MRC university grant to theMRC Human Genetics Unit). PM, MST provided scientific direction and edited the manuscript. LB funded the project, designed and performed experiments and wrote the manuscript. **Acknowledgement:** We would like to thank Prof Roland Rad for his provision of the SB-CRISPR plasmid and Dr Diego Calvesi for providing the Kras^{G12D}-GFP plasmids.

References:

1. Banales JM, Marin JJG, Lamarca A, Rodrigues PM, Khan SA, Roberts LR, et al. Cholangiocarcinoma 2020: the next horizon in mechanisms and management. *Nat Rev Gastroenterol Hepatol*. 2020 Sep;17(9):557–588.
2. Valle JW, Kelley RK, Nervi B, Oh D-Y, Zhu AX. Biliary tract cancer. *Lancet*. 2021 Jan 30;397(10272):428–444.
3. Adeva J, Sangro B, Salati M, Edeline J, La Casta A, Bittoni A, et al. Medical treatment for cholangiocarcinoma. *Liver Int*. 2019 May;39 Suppl 1:123–142.
4. Petmitr S, Pinlaor S, Thousungnoen A, Karalak A, Migasena P. K-ras oncogene and p53 gene mutations in cholangiocarcinoma from Thai patients. *Southeast Asian J Trop Med Public Health*. 1998 Mar;29(1):71–75.
5. Hill MA, Alexander WB, Guo B, Kato Y, Patra K, O’Dell MR, et al. Kras and Tp53 Mutations Cause Cholangiocyte- and Hepatocyte-Derived Cholangiocarcinoma. *Cancer Res*. 2018 Aug 15;78(16):4445–4451.
6. Goepfert B, Folseraas T, Roessler S, Kloor M, Volckmar A-L, Endris V, et al. Genomic characterization of cholangiocarcinoma in primary sclerosing cholangitis reveals therapeutic opportunities. *Hepatology*. 2020 Aug 19;72(4):1253–1266.
7. Zou S, Li J, Zhou H, Frech C, Jiang X, Chu JSC, et al. Mutational landscape of intrahepatic cholangiocarcinoma. *Nat Commun*. 2014 Dec 15;5:5696.
8. Chan-On W, Nairismägi M-L, Ong CK, Lim WK, Dima S, Pairojkul C, et al. Exome sequencing identifies distinct mutational patterns in liver fluke-related and non-infection-related bile duct cancers. *Nat Genet*. 2013 Dec;45(12):1474–1478.
9. Jusakul A, Cutcutache I, Yong CH, Lim JQ, Huang MN, Padmanabhan N, et al. Whole-Genome and Epigenomic Landscapes of Etiologically Distinct Subtypes of Cholangiocarcinoma. *Cancer Discov*. 2017 Oct;7(10):1116–1135.
10. Gonzalez-Perez A, Perez-Llamas C, Deu-Pons J, Tamborero D, Schroeder MP, Jene-Sanz A, et al. IntOGen-mutations identifies cancer drivers across tumor types. *Nat Methods*. 2013 Nov;10(11):1081–1082.
11. Sia D, Losic B, Moeini A, Cabellos L, Hao K, Revill K, et al. Massive parallel sequencing uncovers actionable FGFR2-PPHLN1 fusion and ARAF mutations in intrahepatic cholangiocarcinoma. *Nat Commun*. 2015 Jan 22;6:6087.
12. Shalem O, Sanjana NE, Hartenian E, Shi X, Scott DA, Mikkelsen T, et al. Genome-scale CRISPR-Cas9 knockout screening in human cells. *Science*. 2014 Jan 3;343(6166):84–87.
13. Read A, Gao S, Batchelor E, Luo J. Flexible CRISPR library construction using parallel oligonucleotide retrieval. *Nucleic Acids Res*. 2017 Jun 20;45(11):e101.
14. Ewels PA, Peltzer A, Fillinger S, Patel H, Alneberg J, Wilm A, et al. The nf-core framework for community-curated bioinformatics pipelines. *Nat Biotechnol*. 2020 Mar;38(3):276–278.

15. Thorvaldsdóttir H, Robinson JT, Mesirov JP. Integrative Genomics Viewer (IGV): high-performance genomics data visualization and exploration. *Brief Bioinformatics*. 2013 Mar;14(2):178–192.
16. Rios AC, Capaldo BD, Vaillant F, Pal B, van Ineveld R, Dawson CA, et al. Intraclonal Plasticity in Mammary Tumors Revealed through Large-Scale Single-Cell Resolution 3D Imaging. *Cancer Cell*. 2019 Apr 15;35(4):618–632.e6.
17. Sriskandarajah P, De Haven Brandon A, MacLeod K, Carragher NO, Kirkin V, Kaiser M, et al. Combined targeting of MEK and the glucocorticoid receptor for the treatment of RAS-mutant multiple myeloma. *BMC Cancer*. 2020 Mar 30;20(1):269.
18. Lowery MA, Burris HA, Janku F, Shroff RT, Cleary JM, Azad NS, et al. Safety and activity of ivosidenib in patients with IDH1-mutant advanced cholangiocarcinoma: a phase 1 study. *Lancet Gastroenterol Hepatol*. 2019 Jul 9;4(9):711–720.
19. Javle MM, Borbath I, Clarke SJ, Hitre E, Louvet C, Mercade TM, et al. Infigratinib versus gemcitabine plus cisplatin multicenter, open-label, randomized, phase 3 study in patients with advanced cholangiocarcinoma with FGFR2 gene fusions/translocations: The PROOF trial. *JCO*. 2019 May 20;37(15_suppl):TPS4155–TPS4155.
20. Bekaii-Saab TS, Bridgewater J, Normanno N. Practical considerations in screening for genetic alterations in cholangiocarcinoma. *Ann Oncol*. 2021 Apr 28;
21. Nakamura H, Arai Y, Totoki Y, Shiota T, Elzawahry A, Kato M, et al. Genomic spectra of biliary tract cancer. *Nat Genet*. 2015 Sep;47(9):1003–1010.
22. Farshidfar F, Zheng S, Gingras M-C, Newton Y, Shih J, Robertson AG, et al. Integrative Genomic Analysis of Cholangiocarcinoma Identifies Distinct IDH-Mutant Molecular Profiles. *Cell Rep*. 2017 Jun 27;19(13):2878–2880.
23. Wu G, Feng X, Stein L. A human functional protein interaction network and its application to cancer data analysis. *Genome Biol*. 2010 May 19;11(5):R53.
24. Newman MEJ. Modularity and community structure in networks. *Proc Natl Acad Sci USA*. 2006 Jun 6;103(23):8577–8582.
25. Dong L-Q, Shi Y, Ma L-J, Yang L-X, Wang X-Y, Zhang S, et al. Spatial and temporal clonal evolution of intrahepatic cholangiocarcinoma. *J Hepatol*. 2018 Mar 16;69(1):89–98.
26. Weber J, Öllinger R, Friedrich M, Ehmer U, Barenboim M, Steiger K, et al. CRISPR/Cas9 somatic multiplex-mutagenesis for high-throughput functional cancer genomics in mice. *Proc Natl Acad Sci USA*. 2015 Nov 10;112(45):13982–13987.
27. Wang J, Dong M, Xu Z, Song X, Zhang S, Qiao Y, et al. Notch2 controls hepatocyte-derived cholangiocarcinoma formation in mice. *Oncogene*. 2018 Jun;37(24):3229–3242.
28. Fan B, Malato Y, Calvisi DF, Naqvi S, Razumilava N, Ribback S, et al. Cholangiocarcinomas can originate from hepatocytes in mice. *J Clin Invest*. 2012 Aug;122(8):2911–2915.
29. Tennant PA, Foster RG, Dodd DO, Sou IF, McPhie F, Younger N, et al. Fluorescent *in vivo* editing reporter (FIVER): A novel multispectral reporter of *in vivo* genome editing. *BioRxiv*. 2020 Jul 14;

30. Kang T-W, Yevsa T, Woller N, Hoenicke L, Wuestefeld T, Dauch D, et al. Senescence surveillance of pre-malignant hepatocytes limits liver cancer development. *Nature*. 2011 Nov 9;479(7374):547–551.
31. Morton JP, Timpson P, Karim SA, Ridgway RA, Athineos D, Doyle B, et al. Mutant p53 drives metastasis and overcomes growth arrest/senescence in pancreatic cancer. *Proc Natl Acad Sci USA*. 2010 Jan 5;107(1):246–251.
32. Kim M, Kim S, Lee SH, Kim W, Sohn MJ, Kim HS, et al. Merlin inhibits Wnt/ β -catenin signaling by blocking LRP6 phosphorylation. *Cell Death Differ*. 2016 Jun 10;23(10):1638–1647.
33. Malhotra S, Wood J, Mansy T, Singh R, Zaitoun A, Madhusudan S. Intrahepatic Sarcomatoid Cholangiocarcinoma. *J Oncol*. 2010;2010:1–4.
34. Kim DK, Kim BR, Jeong JS, Baek YH. Analysis of intrahepatic sarcomatoid cholangiocarcinoma: Experience from 11 cases within 17 years. *World J Gastroenterol*. 2019 Feb 7;25(5):608–621.
35. Boulter L, Guest RV, Kendall TJ, Wilson DH, Wojtacha D, Robson AJ, et al. WNT signaling drives cholangiocarcinoma growth and can be pharmacologically inhibited. *J Clin Invest*. 2015 Mar 2;125(3):1269–1285.
36. Guichard C, Amaddeo G, Imbeaud S, Ladeiro Y, Pelletier L, Maad IB, et al. Integrated analysis of somatic mutations and focal copy-number changes identifies key genes and pathways in hepatocellular carcinoma. *Nat Genet*. 2012 May 6;44(6):694–698.
37. Sato K, Murai H, Ueda Y, Katsuda S. Intrahepatic sarcomatoid cholangiocarcinoma of round cell variant: a case report and immunohistochemical studies. *Virchows Arch*. 2006 Nov;449(5):585–590.
38. Mah KM, Houston DW, Weiner JA. The γ -Protocadherin-C3 isoform inhibits canonical Wnt signalling by binding to and stabilizing Axin1 at the membrane. *Sci Rep*. 2016 Aug 17;6:31665.
39. O'Rourke CJ, Matter MS, Nepal C, Caetano-Oliveira R, Ton PT, Factor VM, et al. Identification of a Pan-Gamma-Secretase Inhibitor Response Signature for Notch-Driven Cholangiocarcinoma. *Hepatology*. 2020;71(1):196–213.
40. Carnero A, Blanco-Aparicio C, Renner O, Link W, Leal JFM. The PTEN/PI3K/AKT signalling pathway in cancer, therapeutic implications. *Curr Cancer Drug Targets*. 2008 May;8(3):187–198.
41. Xu X, Kobayashi S, Qiao W, Li C, Xiao C, Radaeva S, et al. Induction of intrahepatic cholangiocellular carcinoma by liver-specific disruption of Smad4 and Pten in mice. *J Clin Invest*. 2006 Jul;116(7):1843–1852.
42. Chen J, Debebe A, Zeng N, Kopp J, He L, Sander M, et al. Transformation of SOX9+ cells by Pten deletion synergizes with steatotic liver injury to drive development of hepatocellular and cholangiocarcinoma. *Sci Rep*. 2021 Jun 3;11(1):11823.
43. Guest RV, Boulter L, Dwyer BJ, Kendall TJ, Man T-Y, Minnis-Lyons SE, et al. Notch3 drives development and progression of cholangiocarcinoma. *Proc Natl Acad Sci USA*. 2016 Oct 25;113(43):12250–12255.

44. Dawson CA, Pal B, Vaillant F, Gandolfo LC, Liu Z, Bleriot C, et al. Tissue-resident ductal macrophages survey the mammary epithelium and facilitate tissue remodelling. *Nat Cell Biol.* 2020 May;22(5):546–558.
45. Wang P, Song X, Utpatel K, Shang R, Yang YM, Xu M, et al. MEK inhibition suppresses K-Ras wild-type cholangiocarcinoma in vitro and in vivo via inhibiting cell proliferation and modulating tumor microenvironment. *Cell Death Dis.* 2019 Feb 11;10(2):120.
46. Cui Y, Groth S, Troutman S, Carlstedt A, Sperka T, Riecken LB, et al. The NF2 tumor suppressor merlin interacts with Ras and RasGAP, which may modulate Ras signaling. *Oncogene.* 2019 Jul 16;38(36):6370–6381.
47. Benhamouche-Trouillet S, O’Loughlin E, Liu C-H, Polacheck W, Fitamant J, McKee M, et al. Proliferation-independent role of NF2 (merlin) in limiting biliary morphogenesis. *Development.* 2018 Apr 30;145(9).
48. Attisano L, Wrana JL. Signal integration in TGF- β , WNT, and Hippo pathways. *F1000Prime Rep.* 2013 Jun 3;5:17.
49. Monga SP. β -Catenin Signaling and Roles in Liver Homeostasis, Injury, and Tumorigenesis. *Gastroenterology.* 2015 Jun;148(7):1294–1310.
50. Qiao Y, Wang J, Karagoz E, Liang B, Song X, Shang R, et al. Axis inhibition protein 1 (Axin1) Deletion-Induced Hepatocarcinogenesis Requires Intact β -Catenin but Not Notch Cascade in Mice. *Hepatology.* 2019 Dec;70(6):2003–2017.
51. Zhong Z, Sepramaniam S, Chew XH, Wood K, Lee MA, Madan B, et al. PORCN inhibition synergizes with PI3K/mTOR inhibition in Wnt-addicted cancers. *Oncogene.* 2019 Aug 7;38(40):6662–6677.

Figure 1 – In silico screening identifies novel drivers of intrahepatic cholangiocarcinoma: **A.** The number of samples with mutations in driver genes identified following analysis with IntOGen. Samples clustered into those which had been previously identified in ICC or are present in the COSMIC database (yellow points), or those mutated genes that have not previously been assigned as being cancer drivers (blue points). **B.** Frequency of samples containing known ICC or COSMIC mutation in each of the individual cohorts collated in this study and in the pooled datasets and **C.** Frequency of samples containing a predicted novel oncogenic mutation called by IntOGen. In both B and C heat maps represent the frequency at which each mutation is found within each study and the aggregated frequency between all studies. Upper bar represents the number of times a mutation was identified between studies. **D.** Pathway interaction analysis of putative ICC driver mutations identified by IntOGen based on known functional (solid lines) and predicted physical (dotted lines) interactions. Numbers 1-6 represent distinct gene-relationship modules based on predicted or known genetic interactions. **E.** Co-occurrence and mutual exclusivity analysis demonstrates that there is a high level of mutational exclusivity between canonical driver mutations in patients with ICC. **F.** Co-occurrence and mutual exclusivity of COSMIC drivers that co-occur ≥ 15 times in the human sample set and combined “other” which includes all novel drivers. N=277 patient exomes or genomes with matched, non-cancerous tissue.

Figure 2. – In vivo CRISPR-Cas9 screening identifies transforming mutations that interact with mutant Ras. **A.** Schematic of this study in which high content sequencing data is collated from patients with ICC and the mutational profile of these tumours rationalised to identify novel, high confidence drivers of ICC. These putative drivers are used as input for an *in vivo* SpCas9/CRISPR screen to identify novel functional processes that drive ICC growth. **B.** Macroscopic images of the livers following injection with either NRAS^{G12V} or KRAS^{G12D} alone (left-hand images) or in combination with ICC^{Lib}, right-hand images, dotted line denotes tumour (scale bar = 1 cm). **C.** Quantification of macroscopic tumours per mouse at 10 weeks in mice bearing Nras^{G12V} expressing tumours and 8 weeks in those with Kras^{G12D}-driven cancer. Each circle represents a different animal. **D.** The number of samples containing Indels in a particular gene following whole exome sequencing. Upper graph lists those mutations found in both NRAS^{G12V} and KRAS^{G12D} tumours, and lower graphs denote those mutations that are found only in KRAS^{G12D} or NRAS^{G12V} expressing tumours. Sample frequency (%) denotes the proportion of tumours containing any given mutation, whereas (count) is absolute number. (N represents anatomically discreet tumours recovered from at least four individual animals, KRAS^{G12D} N=14 and NRAS^{G12V} N=10). **E.** Principal Component Analysis showing how samples group based on their transcriptomic signature and gRNA-induced mutations associated with each tumour type.

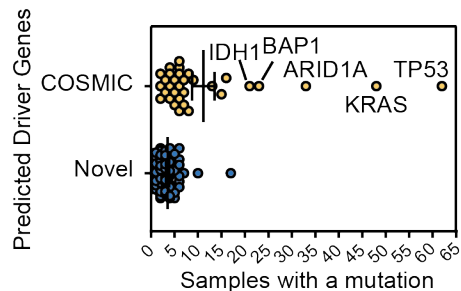
Figure 3 – Nf2-loss results in Ras^{G12D}-induced oncogenesis and cooperates with Trp53-loss to accelerate ICC formation. **A.** Kaplan-Meier curve demonstrating the relative survival proportions of mice with KRAS^{G12D} and gRNAs targeting *Trp53* (N=12), *Nf2* (N=5), *Nf2;Trp53* (N=13) or non-targeting control (scrm, N=5). **B.** Proportion of liver occupied by tumour and **C.** number of tumours per mouse. **D.** H&E staining of KRAS^{G12D} tumours with *Trp53*, *Nf2* or *Trp53* and *Nf2*-loss, scale bar = 100 μ m, dotted line denotes tumour-stroma boundary. **E.** Comparison of RNAseq analysis when the transcriptomes from *Nf2;Trp53* vs *Trp53*-alone tumours (blue) are compared to transcripts from *Nf2;Trp53* vs *Nf2*-alone (yellow) tumours. Each group contains N=4 regionally distinct tumours. **F.** Analysis of RPPA data demonstrating the changes in the proportion of phosphorylated GSK3 α/β , β -catenin and pAKT relative to total protein levels in KRAS^{G12D};*Trp53*^{KO} (grey points), KRAS^{G12D};*Nf2*^{KO} (yellow points), KRAS^{G12D};*Trp53*^{KO};*Nf2*^{KO} (blue points). **G.** Immunohistochemistry of active, dephosphorylated β -catenin (upper panels) and phosphorylated AKT^{Ser647} (lower panels) in KRAS^{G12D};*Trp53*^{KO}, KRAS^{G12D};*Nf2*^{KO}, KRAS^{G12D};*Trp53*^{KO}/*Nf2*^{KO} tumours. Scale bar = 50 μ m **H.** Immunoblot

for dephosphorylated (active) β -catenin (β -catenin^{Ser33/37/Thr41}) in tumours isolated from mice bearing $Kras^{G12D}$ driven ICC with *Trp53*, *Nf2* or *Trp53;Nf2* co-loss. GAPDH is used as a loading control. **I.** Schematic representing our dosing approach to determine whether Wnt inhibition, PI3K inhibition or a combination of the two is effective in improving the survival of mice with $KRAS^{G12D};Trp53^{KO};Nf2^{KO}$ ICC. **J.** Kaplan-Meier curve demonstrating the survival changes when $KRAS^{G12D};Trp53^{KO};Nf2^{KO}$ animals are treated with vehicle (yellow line), LGK974 (Wnt-inhibitor, blue line), Pictilisib (PI3K inhibitor, orange line) or a combination (green line). N=5 per group.

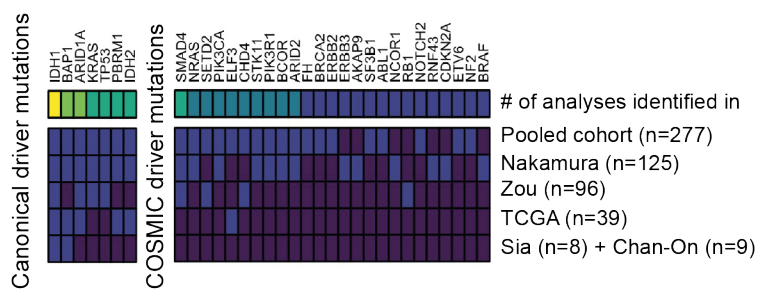
Figure 4: Therapeutic co-inhibition of Wnt and PI3K signalling reduces tumour growth in ICC. A. RNA sequencing data of human ICC demonstrating a positive correlation between the activity of canonical Wnt signalling and Akt signalling. **B.** Schematic representation of the KPPTom cholangiocarcinoma model where Cre^{ERT} expression in Keratin-19-positive cholangiocytes results in the inactivation of *Trp53* and *Pten*, whilst labelling transformed cells with tdTomato. **C.** Representative Immunohistochemical staining of KPPTom model following tamoxifen administration (day 0) and following 4 and 8 weeks of thioacetamide administration. tdTomato (red) denotes recombined cholangiocytes (denoted by Keratin-19, green). DNA is blue. Upper images show whole mount FUNGI images and lower, 2D histological sections. Scale bar=200 μ m, white arrows denote tdTomato positive cells. **D.** Quantification of liver tissue occupied by tumour in the KPPTom ICC model. **E.** Immunohistochemistry showing that KPPTom ICC has activated canonical Wnt signalling (by staining for dephosphorylated (active) β -catenin) and PI3K activity (through pAKT^{Ser647} positivity). Red arrows denote positive cells. Scale bar = 100 μ m. **F.** A schematic representation of how the KPPTom model was used to test the effectiveness of Wnt and Pi3K inhibitor combinations on ICC progression. **G.** Immunohistochemical staining for tdTomato positive cancer cells in vehicle treated animals compared to those treated with a combination of LGK974 and Pictilisib. Scale bar = 100 μ m. **H.** Number of tdTomato positive cells in KPPTom animals given vehicle or LGK974 and Pictilisib in combination. **I.** Proportion of KPPTom animals containing macroscopic tumours in KPPTom animals treated with vehicle vs combination treatment. b.d. – bile duct, p.v. – portal vein

Figure 1

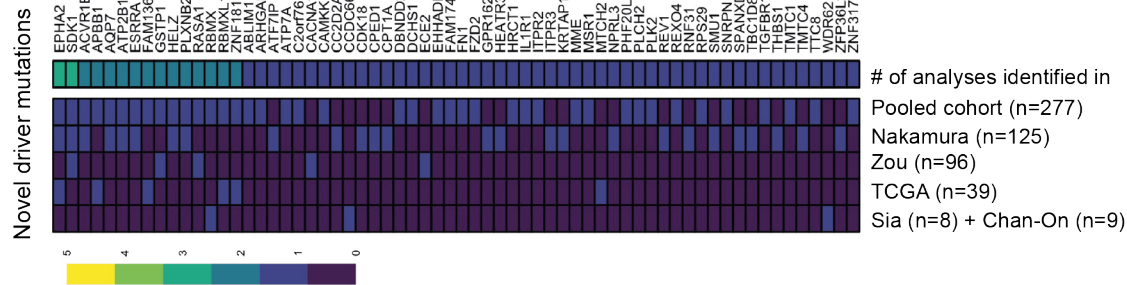
A



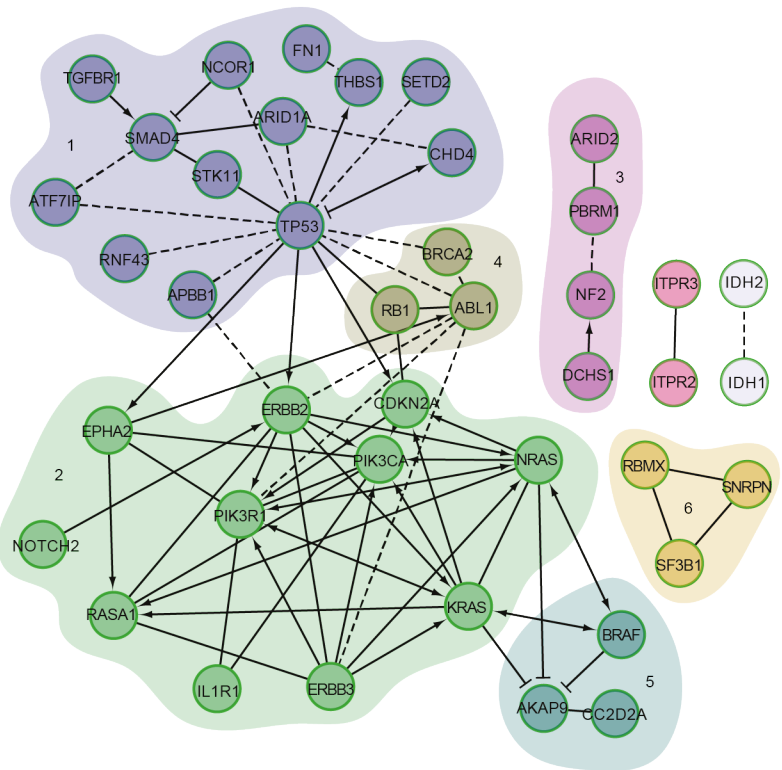
B



C



D



E

	ARID1A	BAP1	IDH1	IDH2	KRAS	PBRM1	TP53
ARID1A	36	6 6.2	5 5.3	0 1.9	9 11.6	5 5.1	5 12.2
BAP1		27	6 4	2 1.4	2 8.8	4 3.9	1 9.3
IDH1			23	2 1.1	1 7.5	2 3.3	1 7.7
IDH2	*			8	0 2.5	2 1.1	0 2.8
KRAS		*	*	*	50	2 7.2	17 17
PBRM1					*	22	2 7.6
TP53	*	*	*	*		*	53

F

	other	cosmic	ARID1A	BAP1	BRAF	EPHA2	IDH1	KRAS	PBRM1	PIK3CA	SMAD4	TP53
other	173	85 83.8	26 26.3	24 19.8	10 10.9	18 14	17	29 36.6	19 16.1	8 11	14 11.7	32 38.9
cosmic		114	18 17.5	13 13.2	10 7.3	9 9.3	9 11.1	17 24	13 10.6	7 7.2	8 7.8	27 25.5
ARID1A			36	6 4.1	3 2.2	5 2.9	5 3.6	9 7.6	5 3.3	5 2.3	5 2.5	5 8.1
BAP1				27	1 1.8	2 2.1	6 2.6	2 5.8	4 2.5	4 1.7	0 1.7	1 6
BRAF					15	4 1.2	3 1.4	2 3.2	1 0.9	2 1.1	2 3.3	7 7
EPHA2	*					19	5 1.8	4 4.1	2 1.7	1 1.3	1 1.3	4 4.3
IDH1							23	1 4.9	2 1.4	3 1.5	0 1.5	1 5.2
KRAS	*	*						50	4 4.5	3 3.4	8 8	17 11.4
PBRM1									22	2 1.5	0 1.5	2 4.9
PIK3CA										15	1 1	4 3.3
SMAD4											16	5 3.6
TP53	*	*	*	*		*						53

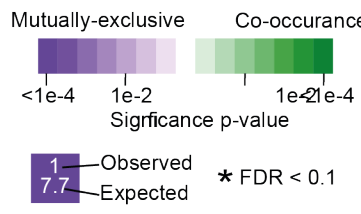
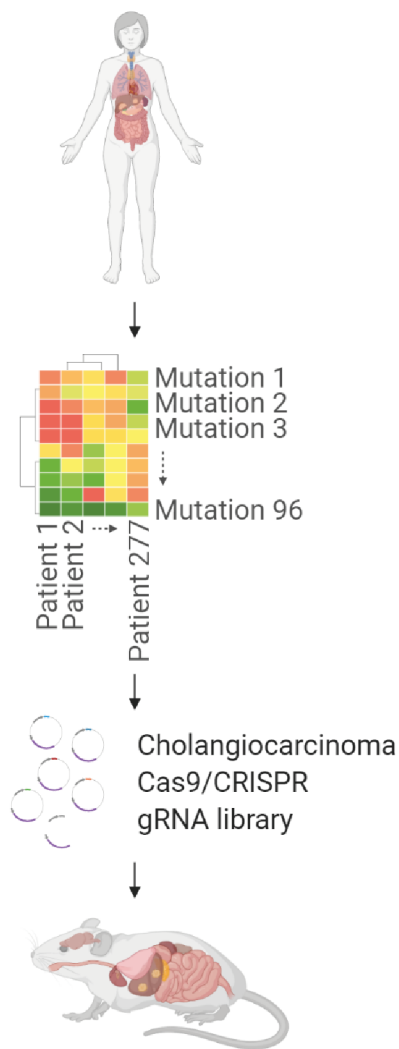
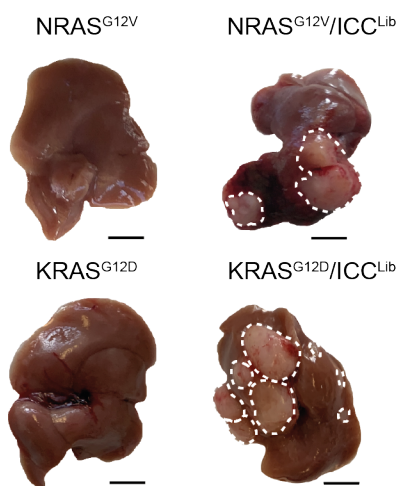


Figure 2

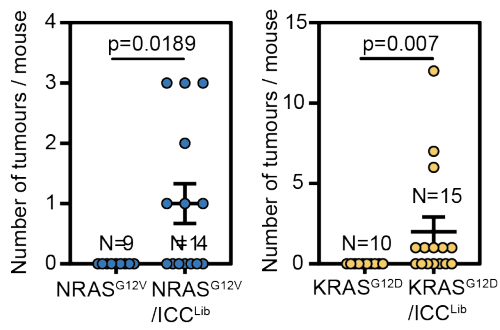
A



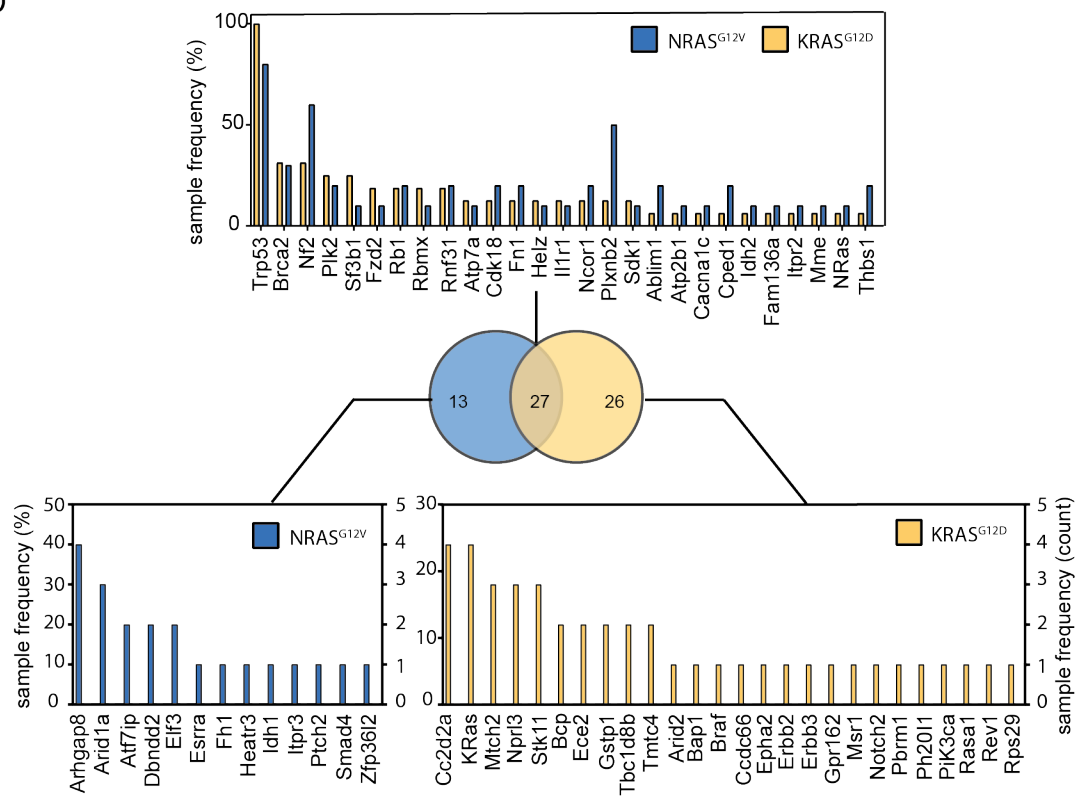
B



C



D



E

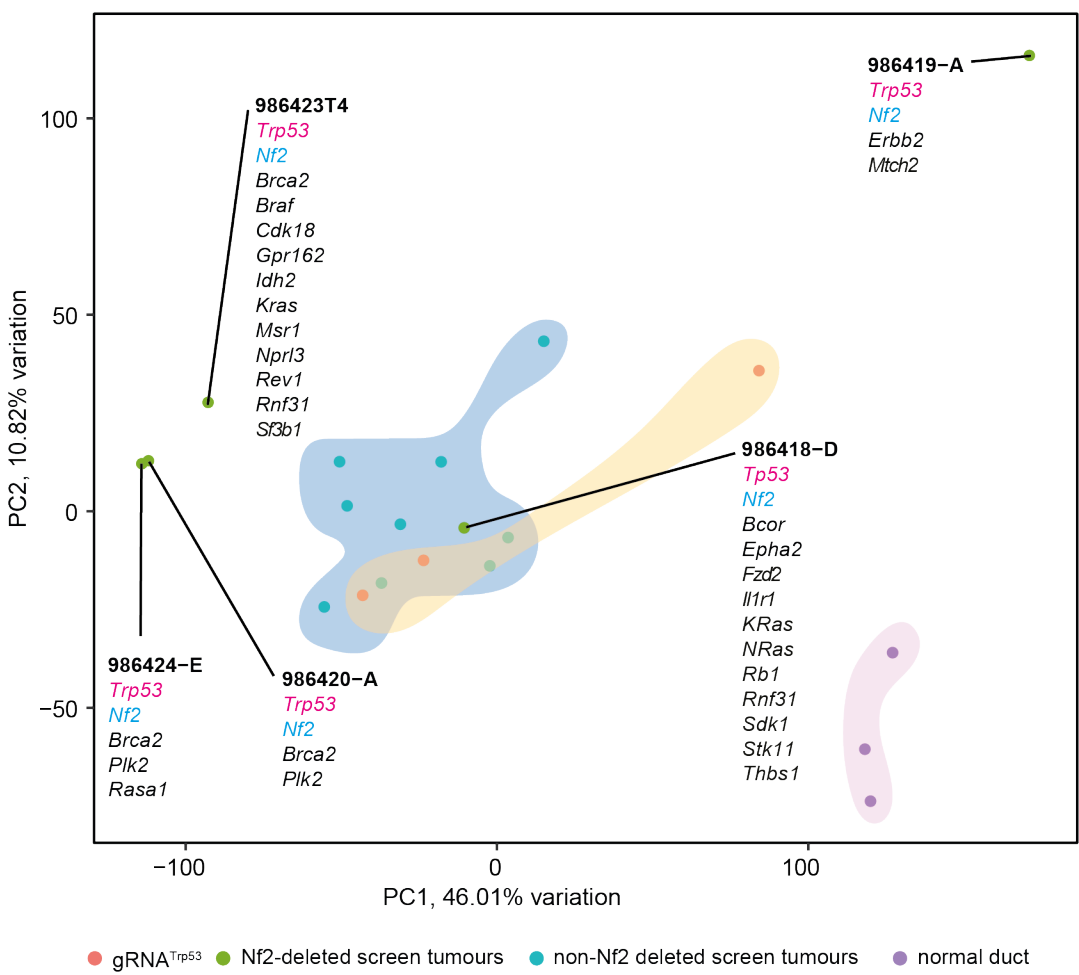


Figure 3

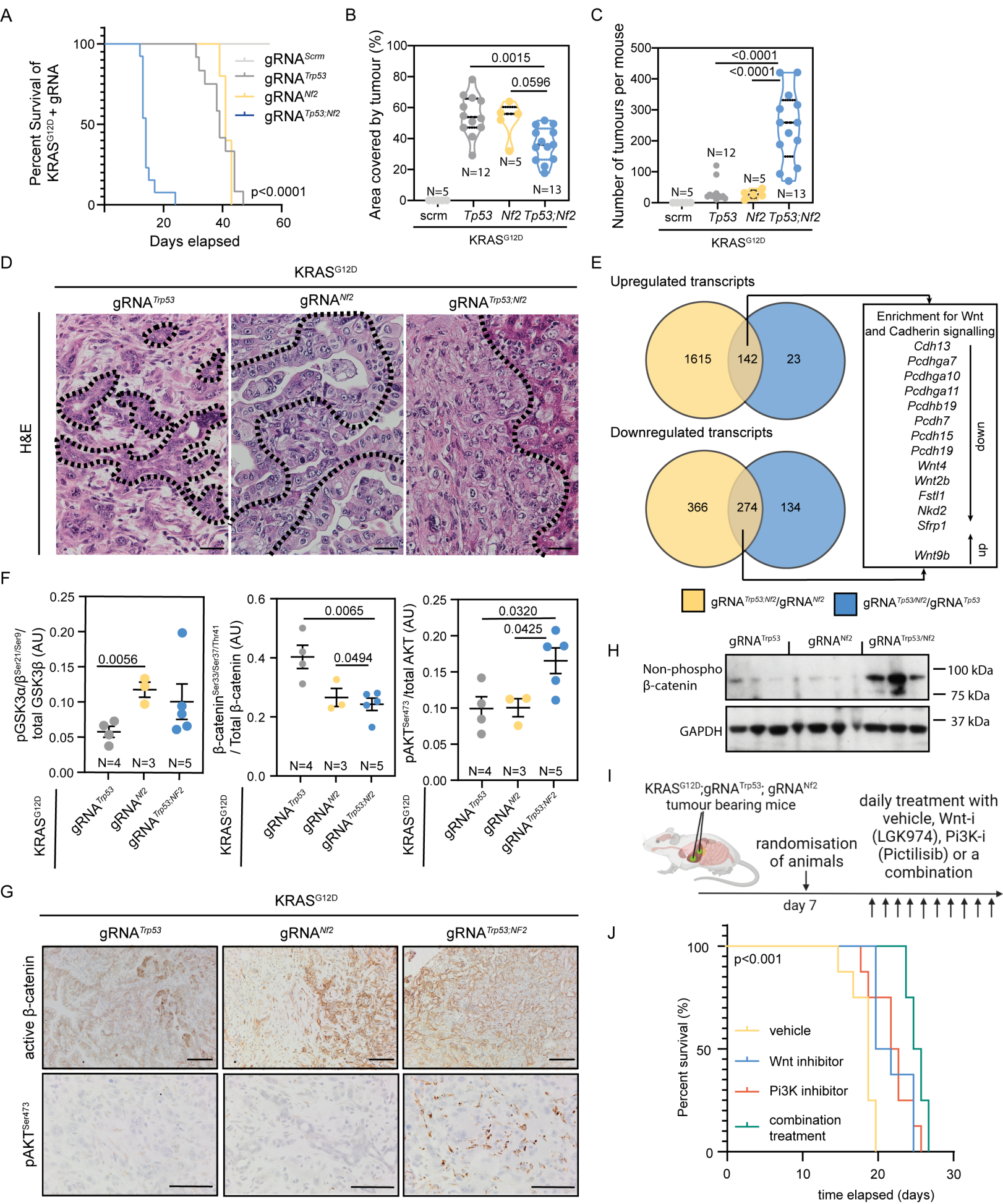


Figure 4

